PHOTONICS Research

Demonstration of a photonic integrated circuit for quantitative phase imaging

Chupao Lin,[1,2,3] Yujie Guo,[1,2] and Nicolas Le Thomas[1,2,4]

[1]Photonics Research Group, INTEC Department, Ghent University-imec, 9052 Ghent, Belgium
[2]Center for Nano- and Biophotonics, Ghent University, 9052 Ghent, Belgium
[3]e-mail: Chupao. Lin@UGent.be
[4]e-mail: Nicolas. LeThomas@UGent.be

Received 11 March 2024; revised 2 September 2024; accepted 15 October 2024; posted 16 October 2024 (Doc. ID 523534); published 16 December 2024

Quantitative phase imaging (QPI) is an optical microscopy method that has been developed over nearly a century to rapidly visualize and analyze transparent or weakly scattering objects in view of biological, medical, or material science applications. The bulky nature of the most performant QPI techniques in terms of phase noise limits their large-scale deployment. In this context, the beam shaping properties of photonic chips, combined with their intrinsic compact size and low cost, could be beneficial. Here, we demonstrate the implementation of QPI with a photonic integrated circuit (PIC) used as an add-on to a standard wide-field microscope. Combining a 50 mm × 50 mm footprint PIC as a secondary coherent illuminating light source with an imaging microscope objective of numerical aperture 0.45 and implementing a phase retrieval approach based on the Kramers–Kronig relations, we achieve a phase noise of 5.5 mrad and a diffraction limited spatial resolution of 400 nm. As a result, we retrieve quantitative phase images of *Escherichia coli* bacteria cells and monolayers of graphene patches from which we determine a graphene monolayer thickness of 0.45 ± 0.15 nm. The current phase noise level is more than five times lower than that obtained with other state-of-the-art QPI techniques using coherent light sources and comparable to their counterparts based on incoherent light sources. The PIC-based QPI technique opens new avenues for low-phase noise, miniature, robust, and cost-effective quantitative phase microscopy. ©2024 Chinese Laser Press

https://doi.org/10.1364/PRJ.523534

1. INTRODUCTION

Shaping light beams, namely the process of engineering the irradiance and the wavefront of an optical radiation, is fundamental to many, if not all, optical applications. This is traditionally implemented with conventional free-space and bulky optics such as mirrors, optical lenses, and diffractive diffusers and more advanced components such as spatial light modulators [1,2]. The bulky nature of these components and of their combinations, the size of which is more than five orders of magnitude larger than the wavelength of the beam, imposes harsh alignment and stability constraints, which leads to limited performance even for applications where the cost is not a real limiting factor. In this context, photonic integrated circuits (PICs) are promising solutions to outperform conventional optical systems and provide new opportunities for beam shaping by taking advantage of their compatibility with complementary metal oxide semiconductor (CMOS) technology. PICs are able to shape and control optical beams in a compact and robust way. When optical phase arrays [3,4] are included in the PICs, they can be used, for instance, for reliable, low-power, and affordable light detection and ranging (LiDAR) applications [5] for image classification [6] or spaced-based optical communications terminals [7]. PICs designs that are less demanding in terms of the impact of residual fabrication errors than the aforementioned examples can already offer new functionalities, as recently unveiled for super-resolved near-field [8,9] and far-field [10,11] structured illumination microscopy, on-chip ion trapping for quantum computing [12], laser beam scanning [13], and optogenetic probes [14]. Here, we present a novel conceptual application of PICs that allows us to significantly outperform state-of-the-art coherent light source-based quantitative phase imaging (QPI) techniques that make use of bulky optical components or of compact metasurfaces. Our technique that works with coherent light provides a phase noise level comparable to the best one obtained with incoherent light sources. We take advantage of the integration and design flexibility of photonic integrated circuits to dynamically match their far-field emission pattern with specific positions at the aperture stop of a given imaging microscope objective. This approach allows us to implement low-phase noise quantitative phase imaging that makes use of the space-domain

Kramers-Kronig (KK) relations, which was first implemented in electron microscopy [15] and recently extended for two-dimensional light microscopy [16]. The photonic integrated circuit provides the illumination beam required for taking advantage of the KK relations without any reshaping of the exit pupil of the collecting microscope objective. As a main result, we show that the compact nature of the PICs leads to a seven times improvement of the phase noise compared to the KK-based approach using conventional free-space optics and enables to image graphene monolayers with high contrast.

2. PRINCIPLE OF PIC-BASED QPI TECHNIQUE

One of the main challenges to make quantitative phase imaging a powerful label-free method for investigating the morphology and refractive index of transparent objects is the phase stability of the instrument [17]. Any mechanical vibrations or air fluctuations along the optical path result in phase noise that spoils the image contrast. To mitigate this problem, several common-path approaches [16,18–21] have been proposed. In these configurations, the illuminating beam that is incident on the sample serves as the phase reference and follows the same optical path as the field scattered by the object. As the reference and scattered beam are subject to almost the same phase fluctuations, the noise resulting from these fluctuations is canceled out during the interference process at the camera sensor. In practice, even a common-path configuration is not fully immune to phase noise as the relative position of the illumination beam and of the scattered field has to be stable, as in the KK-based QPI technique discussed below.

Considering an optical microscope objective of a given numerical aperture (NA) and a plane wave illumination of the object with an incident scalar field $E_{\text{in}}(\vec{r})$, as in Fig. 1(a), the scalar spatial field $E(\vec{r})$ in the image plane at a location defined by the position vector $\vec{r} = x\vec{x} + y\vec{y}$ can be described as the sum of the unscattered $E_u(\vec{r})$ and scattered $E_s(\vec{r})$ fields. $E_u(\vec{r})$ corresponds to the fraction of the field that is transmitted through the object with the same transverse wave vector $\vec{k}_{\text{in}}$ as the incident field. The transverse wave vector is defined as the projection of the wave vector in a plane perpendicular to the optical axis (Oz). $E_s(\vec{r})$ results from the scattering process induced by the object. Its angular spectrum includes all the

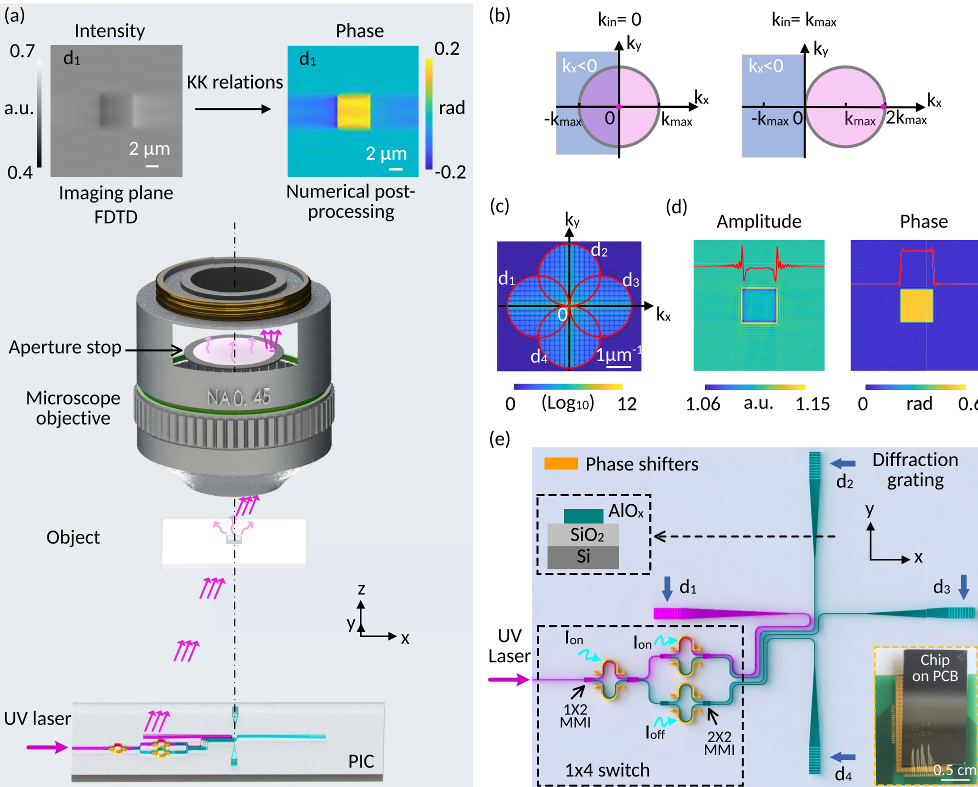

Fig. 1. Working principle of the PIC-based QPI technique. (a) Schematic of the chip-based illumination configuration for quantitative phase imaging. Straight purple arrow, incident beam; wavy light purple arrows, scattered field; top left image, FDTD simulation of the intensity image of the object illuminated with an oblique illumination compatible with the phase retrieval approach based on the Kramer–Kronig relations; top right image, retrieved phase image via numerical post-processing of the top left image. (b) Illustration of the KK-based QPI technique in k-space. Purple disk, aperture of the microscope objective with k_{max} the maximum modulus of the transmitted transverse component of the wave vectors; left, standard normal illumination, with incident transverse k-vector $k_{\text{inc}} = 0$; right, oblique illumination with $k_{\text{inc}} = k_{\text{max}}$, i.e., compatible with the KK relations. (c) Log-scale Fourier domain of the retrieved field image after merging the frequency bands of the four directions of illumination $d_{i=1\text{ to }4}$. (d) Amplitude and phase images obtained by inverse Fourier transform of (c). (e) Schematic of the photonic integrated circuit used in (a) including a cross section of the aluminum oxide waveguide (green). The diffraction gratings provide the oblique illuminations that are switched on (current I_{on}) and off (current I_{off}) with an integrated 1×4 switch made of 1×2 or 2×2 multimode interferometer (MMI) and thermal phase shifters (yellow). Inset: optical image of the entire photonic chip bounded on a PCB board and electrically connected via gold wires.

transverse wave vectors $\vec{k}_s = \vec{k}_x + \vec{k}_y$ other than the incident one and is limited to the spatial bandwidth of the microscope, which is represented, for a wavelength λ, as a disk of radius $k_{\max} = \frac{2\pi}{\lambda}\mathrm{NA}$ in the k-space diagram in Fig. 1(b). The field $E(\vec{r})$ conveys important information about the object, for instance, its shape. In standard quantitative optical microscopy, a digital image sensor records the intensity map $I(\vec{r})$ of the field. It follows that the phase information is lost—and with it the information related to the object's morphology. Many experimental and numerical QPI techniques have been implemented to circumvent this problem, including phase-shifting digital holography microscopy (DHM) [22,23], Fourier phase microscopy [24], gradient light interference microscopy (GLIM) [21], ptychography [25], quantitative oblique back-illumination microscopy [26], and phase retrieval based on the transport-of-intensity equation (TIE) [27]. These approaches rely in general on bulky optical setups that are not ideal for minimizing the phase noise. Recently, miniature QPI interferometric setups have been explored by designing metal gratings on coverslips [28], gratings on fluidic chips [29], and Si-based metasurfaces on fused silica substrates [30,31]. However, the gain in compactness comes at the expense of the general phase noise performance.

The phase noise level depends on the degree of coherence of the light source. Although coherent laser sources offer advantages such as high brightness, low power consumption, and ease of alignment, their high spatial coherence results in strong light speckles that currently limit the phase noise level to ~30 mrad [32]. The state-of-the-art records of phase resolution are achieved with incoherent white light source based QPI techniques, such as diffraction phase microscopy (DPM) [33], quadriwave lateral shearing interferometry (QSLI) [34], and spatial light interference microscopy (SLIM) [35], for which the phase noise is as low as ~3 mrad. Our approach that uses a PIC to shape a coherent light beam in a compact and robust way achieves phase noise levels comparable to those obtained with incoherent light, as demonstrated below.

Among the different QPI techniques, the KK-based approach has several advantages: the illuminating beam acts as the phase reference in a common path configuration and the phase shifting is replaced by beam steering. As unveiled below, combining a PIC-based illumination with this technique can drastically improve the performance. The underlying principle of the technique is based on the following observation: $E(\vec{r})$ can be entirely described either by its intensity $I(\vec{r})$ and phase $\varphi(\vec{r})$ and written as $E(\vec{r}) = \sqrt{I(\vec{r})}e^{i\varphi(\vec{r})}$ or by its quadratures, namely its real $\mathrm{Re}(E(\vec{r}))$ and imaginary $\mathrm{Im}(E(\vec{r}))$ parts. If the Fourier transform of the field is square integrable, holomorphic, and nonzero only in the upper half plane of the complex plane, the quadratures are deduced from each other by a Hilbert transform [36]; the corresponding relationships are also known as the KK relations. It is reasonable to expect a similar link between the intensity and the phase, which is obtained by considering the function $\ln(E(\vec{r})) = \frac{1}{2}\ln I(\vec{r}) + i\varphi(\vec{r})$ as discussed in the 1970s for electron microscopy in Ref. [15].

Two different microscopy configurations have been implemented up to now to fulfill the necessary conditions to apply KK relations, i.e., the conditions to make $\ln(E)$ an analytical signal; see Appendix A for more details on these conditions. The first one consists in illuminating the sample at normal incidence $k_{\mathrm{in}} = 0$, which leads to a k-space bandwidth centered at the origin, and in reshaping the aperture at the back focal plane [15]. The main challenge is to match precisely the mask with the optical axis in order to cancel one of the half-planes in the back focal plane. In addition the mask must be rotated or flipped around the optical axis in order to reconstruct the whole bandwidth of the aperture. Instead of reshaping and moving a mask in the back focal plane, the other approach relies on oblique plane wave illuminations [16]. A plane wave illumination with a given angle θ defined by $k_{\mathrm{in}} = \frac{2\pi}{\lambda}\sin\theta$ implies a $\vec{k}_{\mathrm{in}}$ shift of the bandwidth in the k-space. The main condition to apply KK relations then fulfilled for $k_{\mathrm{in}} = k_{\max}$ as illustrated in Fig. 1(b). Using Cauchy theory and the Cauchy principal value P, the KK relations between the phase and the image follow. For instance, for an illumination along $\vec{k}_{\mathrm{in}} = k_{\mathrm{in}}\vec{x}$, the phase is given by

$$\varphi(x,y) = -\frac{1}{\pi}P\int_{-\infty}^{\infty}\frac{\ln\sqrt{I(x',y)}}{x'-x}\mathrm{d}x' + k_{\mathrm{in}}x. \quad \textbf{(1)}$$

Repeating this phase retrieval methodology for several directions of illumination allows determining the complex Fourier spectrum $\hat{E}(k_x,k_y)$, from which the amplitude and phase images are deduced.

The phase retrieval approach is illustrated in Fig. 1 with finite-difference time-domain simulations (FDTD, Lumerical) in the case of a simple 5 μm × 5 μm square phase object of height 50 nm and refractive index 1.547. Four directions of illumination labeled d_1 to d_4 and symmetric by a 90 deg rotation around the optical axis (Oz) are considered. For all of them, the illumination angle is set at $\theta = 26.74$ deg to match a numerical aperture of NA = 0.45 in line with our experimental setup. The intensity image of the field $E(\vec{r})$ produced by the microscope is simulated with FDTD for the d_1 illumination in Fig. 1(a). From this intensity image, the phase map of $E(\vec{r})$ is obtained by solving Eq. (1), and the outcome is identical to the FDTD simulated phase as it should be; see Fig. 7 in Appendix A. Knowing the intensity and the phase, the Fourier transform of the field $\hat{E}(k_x,k_y)$ is determined within the spatial frequency bandwidth that is defined by the aperture stop of the collecting microscope objective and by the direction of illumination d_1 and is represented in Fig. 1(c) by the disk labeled d_1. After processing the images for the four consecutive illuminations, the total phase domain of $\hat{E}(k_x,k_y)$ is retrieved as shown in Fig. 1(c) where the contribution of each illumination is identified by d_i. The different contributions have overlapping k-areas that are averaged to avoid doubling the signal. An inverse Fourier transform finally leads to the amplitude and phase images in Fig. 1(d). The recovered phase map reproduces the expected phase profile of the object very well, although some ripples are present due to the sharp edges and limited spatial bandwidth of the microscope.

Rotating the illumination beam to reconstruct the synthetic aperture certainly avoids the motion of a mask in the back-focal plane but still requires stringent dynamical mechanical alignments to match the illumination angle with the aperture stop,

which is a tour de force with bulk optics. Using a photonic integrated circuit made of single-mode waveguides such as the one illustrated in Fig. 1(e) alleviates this problem. The illumination is here provided by four first-order Bragg gratings that diffract the light propagating in the circuit out of the chip at a diffraction angle matching the maximal angle collected in the aperture stop of the microscope objective, i.e., satisfying $k_{\text{in}} = k_{\text{max}}$. During phase imaging, the gratings are excited one after the other with an integrated 1 × 4 optical switch made of three Mach–Zehnder interferometers (MZIs), which avoids any mechanical displacement. Each MZI is made of one 1 × 2 multimode interferometer (MMI) at the input to split the light into the two arms of the MZI, one thermal phase shifter in each arm driven by current sources, and one 2 × 2 MMI at the output. All the gratings can also be excited at the same time with a proper setting of the driving current of the different thermal phase shifters in order to align the photonic chip with the microscope objective. Such an alignment is carried out by imaging the exit pupil of the latter and the far-field of the diffracted beams [see Fig. 2(d)] or by looking at the intensity in the imaging plane. The PIC has a typical compact size of 2 cm by 2 cm on a photonic chip that can be used with any standard optical microscope without modification of the collecting part.

In the following, after presenting the properties of the beam shaping and switching of our PICs, we discuss their performances for quantitive phase imaging on test objects. As key examples, we investigate the phase images of monolayer graphene patches and bacterial cells.

3. RESULTS

A. Reaching Less than 0.5% NA Matching Accuracy

Achieving and maintaining the proper matching conditions between the illuminating beam and the pupil of the collecting lens is demanding. A key advantage of the PIC-based approach is the opportunity to fabricate on a single chip several replicas of the same photonic integrated circuit with a parameter tuning sweep assisted by numerical simulations. Such a sweeping strategy effectively mitigates the effects of residual fabrication errors and allows us to select the best circuit post fabrication. Figure 2(a) provides an example where six PICs of identical design but of different grating parameters are present on the same chip.

The circuits are here made of aluminum oxide AlO_x deposited on thermal silicon oxide wafers with an atomic layer deposition technique (ALD). AlO_x thin-films exhibit very good transparency across a broad wavelength range spanning from

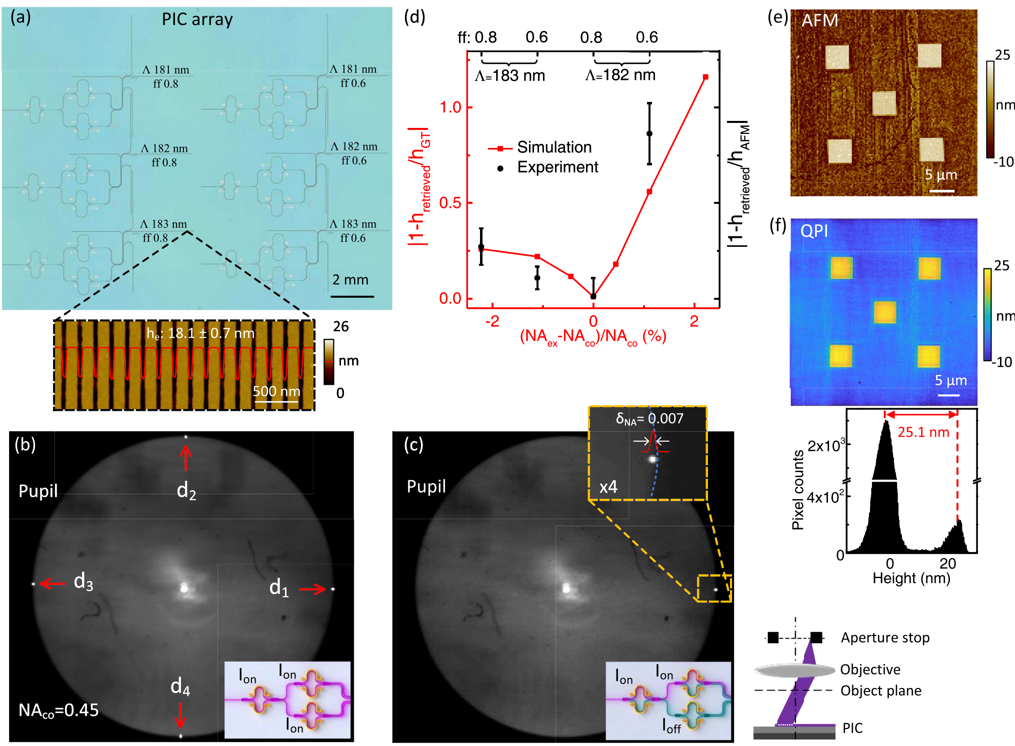

Fig. 2. High-precision control methodology of the beam angle diffracted by the photonic chip. (a) Optical image of a typical photonic chip including six PICs. Zoomed image, atomic force microscopy (AFM) image of one of the shallow etched grating; etch depth, $h_e = 18.1 \pm 0.7$ nm; grating pitch, $\Lambda = 183$ nm; fill factor, ff = 0.8. (b) Optical image of the back focal plane of the microscope objective when all gratings are excited. The clear aperture of the exit pupil is image with a light emitting diode operating at a central wavelength of 370 nm. (c) Optical image of the back focal plane of the microscope objective as in (b) but with only the d_1 oblique illumination. In the zoom-in image $\delta_{\text{NA}} = n \cdot \cos(\theta_{\text{max}}) \cdot \delta_\theta$ indicates the divergence of the beam in unit of NA where θ_{max} is the maximum aperture angle. In (b) and (c), the lower right schematics show the operating state of the integrated optical switch. (d) Relationship between the NA mismatch ratio $(NA_{ex}\text{-}NA_{co})/NA_{co}$ and the retrieved phase error $|1-h_{\text{retrieved}}/h_{\text{GT}}|$ simulated with the FDTD method (red). The experimental data points (black) are obtained with the PICs presented in (a). (e), (f) Topography of a test object imaged by AFM and by the proposed PIC-based QPI technique, respectively. At the bottom of (f), histogram of the height distribution extracted from the QPI image.

ultraviolet-C (UVC) to infrared wavelengths [37–39]. Fully etched single-mode AlO_x waveguides with propagation losses of 3 dB/cm at a wavelength of 360 nm [10,11] are used to guide the light towards the grating out couplers; see Fig. 1(e).

The diffraction gratings play a crucial role in the accuracy of the retrieved phase. The four identical gratings are located on a circle, the center of which corresponds to the position of the optical axis of the microscope objective. The circle has a radius of 2.5 mm. To align the center with the optical axis, the four gratings are simultaneously activated by the guided light, and their far-field emission patterns are imaged in the back-focal plane of the microscope objective; see Fig. 2(b). In the far field, the light diffracted by each grating is similar to a plane wave, which ideally results in a point in the k-space. Each point is indicated in Fig. 2(b) with the corresponding direction of illumination d_i on the image of the exit pupil. The exit pupil is nothing else than a mapping of the k-space. Positioning the four far-field points at the edge of the aperture stop by adjusting the photonic chip guarantees a proper centering of the chip with the collecting microscope objective. With a designed illumination angle corresponding to an excitation numerical aperture of $NA_{ex} = 0.45$, i.e., equal to the specified numerical aperture of the current microscope objective, all the diffracted beams overlap in a plane that is located 4.96 mm above the photonic chip and where the object to be imaged is positioned.

For the rigorous implementation of the KK relations [see Fig. 1(b)] and a subsequent accurate extraction of phase information from the intensity images, precise control of the illumination beam angle is essential as quantified in Fig. 2(d). Simulating images as in Fig. 1(a) with the FDTD method for different angles of illumination and implementing the KK phase imaging approach, it follows that the ratio between the retrieved height $h_{\text{retrieved}}$ of the object and its ground truth value h_{GT} is already increased by more than 20% for a $\pm 1\%$ NA mismatch between the excitation and the collection; see the red curve in Fig. 2(d). A much better accuracy, namely an error of 0.8% between the actual object height and the retrieved height, is obtained experimentally. To achieve such a result we have swept the grating parameters including grating pitches ($\Lambda = 181$, 182, or 183 nm) and filling factors (ff = 0.6 or ff = 0.8) on a single chip with a targeted 20-nm-etch depth in a 120-nm-thick AlO_x layer for all gratings. Mapping the grating surface with an atomic force microscope (AFM) (Park Systems NX20) reveals a grating groove depth h_e of 18.1 ± 0.7 mm in line with the designed value. With the parameter sweep, the illumination angle is tuned from $NA_{ex} = 0.44$ to $NA_{ex} = 0.46$ with a step $\Delta NA_{ex} = 0.005$; see simulation in Fig. 14 in Appendix A.

For each grating, the excitation numerical aperture is experimentally investigated by imaging the exit pupil of the microscope objective. To be able to locate the aperture stop corresponding to the collection numerical aperture $NA_{co} = 0.45$, a light emitting diode (LED) with a central wavelength of 370 nm (LED370E, Thorlabs) illuminates the object in a Köhler configuration. The reflection of the LED illumination by the object provides a signal within all the spatial frequency bandwidth of the microscope objective, which allows relative positioning of the beam diffracted by the grating with respect to the aperture stop; see Figs. 2(d) and 2(c). The 20 μm-wide and 1000-cycles-long diffraction gratings illuminate the object plane over a field of view (FoV) of 210 μm × 187 μm; see Fig. 11 in Appendix A. The corresponding divergence is 0.45 deg, which is retrieved from the beam width $\delta_{\text{NA}} = \text{NA}\frac{\delta k}{k_{\max}} = 0.007$ in the back focal plane; see inset in Fig. 2(c). The current value of the beam divergence is sufficiently small to avoid any bias in the phase retrieval process as discussed with Fig. 8 in Appendix A.

Note that the beam width at half maximum $\delta_{\text{NA}} = 0.007$ is larger than the designed numerical aperture step $\Delta NA_{ex} = 0.005$ between the different circuits, which makes it difficult to experimentally distinguish the difference in illumination angle, i.e., in NA_{ex}, between two consecutive grating designs. In addition, determining the absolute value of NA_{ex} with the accuracy required for the NA mismatch that is here targeted is challenging. Moreover, the actual numerical aperture of the microscope objective might slightly deviate from its specified value of 0.45, which adds another uncertainty. To circumvent these difficulties and provide an experimental value of the NA mismatch, $\Delta NA = (NA_{ex}\text{-}NA_{co})/NA_{co}$, between the illumination and collection, we have determined the phase image of a test phase object and compared the experimentally retrieved height of its profile with the simulated one for different ΔNA. The phase object is made of 5 μm × 5 μm square pillars etched in a 500-nm-thick silicon oxide (SiO_x) layer on a 170-μm-thick microscope cover glass. The nominal etch depth of the pillars is 25 nm. The experimental height of the pillars, $h_{\text{AFM}} = 24.9$ nm, is determined with an AFM measurement and is considered here as ground truth; see Fig. 2(e).

The experimental height $h_{\text{retrieved}}$ retrieved from the KK QPI image in Fig. 2(b) is expected to approach the value h_{AFM} for a given grating design, which is verified by the black dots in Fig. 2(d): $h_{\text{retrieved}} = 25.1$ nm corresponding to a minimum value of $|1\text{–}h_{\text{retrieved}}/h_{\text{AFM}}|$ is achieved for a grating pitch $\Lambda = 182$ nm and a fill factor ff = 0.8. By varying the grating period or the fill factor, FDTD simulations predict that NA_{ex} reaches NA_{co} for a grating pitch of $\Lambda = 183$ nm and a fill factor of ff = 0.8; see Fig. 15(a) in Appendix A. A 1 nm grating pitch step corresponds to a 0.01 NA_{ex} step. This 1-nm-pitch deviation between the simulated and the experimental values results from the combined effect of a 1 nm uncertainty in the AlO_x layer thickness, the 2 nm grating etched depth deviation from the nominal value corresponding to a 0.002 NA_{ex} shift, and a possible uncertainty on the specified NA_{co} value of 0.45. The difference between the simulated grating pitch to obtain the optimal NA matching for KK QPI and the actual experimental value is remarkably less than 0.6%.

The value of $h_{\text{retrieved}}$ is the difference between the average of the distribution of the low heights and the average of the distribution of the high heights in the phase image of Fig. 2(e). The error bars in Fig. 2(d) correspond to the pooled standard deviation σ_p of these two distributions. Taking into one σ_p uncertainty at the minimum NA mismatch and the simulated variations of $|1\text{–}h_{\text{retrieved}}/h_{\text{GT}}|$, a ΔNA accuracy of less than 0.5% is obtained with a height measurement accuracy of 0.8%.

B. Performance of PIC-Based Spatial Phase Imaging

The theoretical spatial transverse resolution of a standard optical microscope is given by $\Lambda_{\min} = \frac{\lambda}{NA_{co}+NA_{ex}}$ for a coherent

plane wave illumination. Λ_{min} corresponds to the smallest period of the optical index modulation that is observable in the imaging plane. At normal incidence, i.e., $\mathrm{NA}_{\mathrm{ex}} = 0$, and for $\mathrm{NA}_{\mathrm{co}} = 0.45$, $\Lambda_{\mathrm{min}} = 800$ nm at an operating wavelength of 360 nm. Under an NA matching condition as used here to implement the KK relations, Λ_{min} decreases to $\frac{\lambda}{2\mathrm{NA}_{\mathrm{co}}} = 400$ nm, namely, two times smaller than that of the conventional normal illumination.

To verify whether the current photonic chip based illumination allows us to reach the 400 nm resolution performance, we have imaged a series of strips with different line spacings that are patterned on a standard cover glass with a nominal height of 46.7 nm. The amplitude and phase images of the strips can be clearly retrieved up to a strip pitch of 400 nm, whereas the three strips with a 300 nm pitch appear as a single strip; see Figs. 3(a) and 3(b). As an important result, the PIC-based illumination allows us to resolve spatial features with the theoretical resolution of the microscope. The current theoretical value can be further improved by using higher NA objectives and by adjusting the PIC design. For instance, decreasing the pitch of the gratings to 150 nm, the diffracted beams will illuminate the object with a high $\mathrm{NA}_{\mathrm{ex}}$ of 0.9, which suggests that imaging phase objects with a spatial resolution of 200 nm is feasible. Theoretically, the maximum achievable NA is constrained by the NA of the microscope objective, which is 0.95 for a dry objective. Achieving a larger illumination NA is possible by using diffraction gratings with a smaller pitch, but it might pose challenges for large-scale fabrication in current foundries, where the typical minimum feature size is 150 nm. Additionally, as the grating pitch decreases, the radius of the circle where the diffraction gratings are positioned must increase to keep the current working distance of 4.96 mm between the sample and the photonic chip. Decreasing further the illumination wavelength will also improve the spatial resolution.

A crucial key performance indicator for the current quantitative phase imaging technique is the standard deviation of the spatial phase noise σ_{φ}, which determines the minimum detectable phase variation. We have used an unpatterned 500-nm-thick silicon oxide layer on top of a flat microscope cover glass to infer σ_{φ}; see Fig. 3(c). The SiO_x layer induces spatial phase fluctuations, the phase distribution of which has a standard deviation as low as $\sigma_{\varphi}^{\mathrm{exp}} = 6.3$ mrad for the entire image. Such a value is up to 7× performance improvement over methods using bulky optics based on KK relationships [40] and up to 13× performance improvement over metasurface-based miniature QPI modules [30].

To disentangle the phase noise contribution intrinsic to the QPI technique from the phase fluctuations induced by the surface roughness of the object, we have mapped the surface topography with an AFM tool and simulated the corresponding KK-based phase image with FDTD; see Fig. 3(d). The AFM scanning of the SiO_x surface provides a root mean square of the height fluctuations of 0.4 nm [see height map histogram in Fig. 3(d)] for an AFM axial resolution of 0.1 nm. It follows that the actual standard deviation of the roughness of the SiO_x layer is $\sigma_{\varphi}^{\mathrm{SiO}_x} = \sqrt{0.4^2 - 0.1^2} = 0.39$ nm. Using the experimental correlation length $l_c^{\mathrm{SiO}_x} = 125$ nm and standard deviation $\sigma_{\varphi}^{\mathrm{SiO}_x} = 0.39$ nm of the surface roughness that are retrieved with the AFM, and simulating the KK-based phase

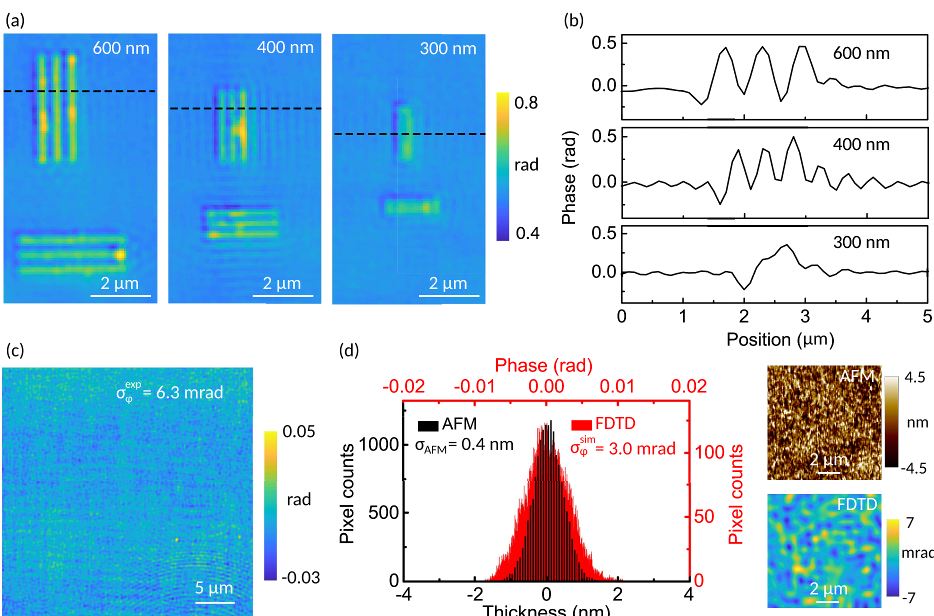

Fig. 3. High spatial resolution and low spatial phase noise. (a) PIC-based QPI images of strips patterns etched in the same glass substrate with spacings of 600 nm, 400 nm, and 300 nm. (b) Cross section of the topological profiles along the dashed black lines in (a). (c) PIC-based QPI image of the surface of a SiO_x layer deposited on a glass substrate. The standard deviation of the phase noise $\sigma_{\varphi}^{\mathrm{exp}} = 6.3$ mrad is determined over the whole image. (d) Left: histogram plots of the fluctuations of the SiO_x surface height measured with AFM and of the associated phase simulated with FDTD. Top right: topographic AFM image. Bottom right: KK-based phase image simulated with FDTD and produced by a surface whose roughness properties are identical to those of the measured AFM image. The root-mean-square (RMS) of the surface roughness $\sigma_{\mathrm{AFM}} = 0.4$ nm and the standard deviation of the phase fluctuations $\sigma_{\varphi}^{\mathrm{sim}} = 3.0$ mrad.

image produced by such a roughness, provides a theoretical standard deviation of the phase fluctuations of $\sigma_\varphi^{\text{sim}} = 3.0$ mrad, which is two times smaller than the experimental data $\sigma_\varphi^{\text{exp}} = 6.3$ mrad measured in Fig. 3(c). Assuming that the phase noise contribution coming from the sample roughness and the one coming from residual imperfections of the experimental setup are uncorrelated, the one-sigma uncertainty on the phase noise that is intrinsic to the QPI technique is $\sigma_\varphi = \sqrt{6.3^2 - 3.0^2} = 5.5$ mrad. To confirm this low noise value and demonstrate the ultimate performance of our approach, we have investigated two-dimensional (2D) materials consisting of a single atomic monolayer.

C. Topography of Two-Dimensional Monoatomic Layers

Two-dimensional (2D) materials, featuring atomic thickness and van der Waals layered structures, have recently attracted much attention in microelectronics and optoelectronics due to their broadband high absorption, ultrafast carrier dynamics, strong mechanical durability, and dangling-bond-free surface nature [41–44]. Importantly, the band structure and electronic and optical properties of graphene and 2D semiconductors are critically dependent on the number of the layers, offering additional freedom for device tunability and scalability. It follows that quantifying precisely the number of layers of a few-layer 2D material is fundamental for understanding its physical properties and practical applications. The two typical ways to distinguish spatially monolayer from bilayer materials are Raman spectroscopy imaging and thickness measurement using AFM. Both techniques involve a time-consuming scanning technique. In contrast, using quantitative phase imaging to characterize 2D materials offers significant time and simplicity benefits provided that the detection limit is sufficient. In Fig. 4(a) we show that the spatial phase noise of our PIC-based QPI approach is low enough to image with high contrast monolayer graphene. With the spatial phase noise of 5.5 mrad previously determined, the QPI one-sigma axial resolution that varies according to the refractive index value and the illumination angle (see Appendix A.6) reaches 0.14 nm for monolayer graphene, the refractive index of which is 3.10 [45].

The monolayer graphene was grown by chemical vapor deposition (CVD), patterned, and transferred to cover glass; see details in Appendix A. The contrast in Fig. 4(a) allows us to clearly identify the patterned monolayer graphene. The high-phase value at the horizontal edges of the graphene patch may be caused by an imperfect adhesion on the glass substrate. The cross section along the dashed black line in Fig. 4(a) is plotted in Fig. 4(b) to quantify the thickness of the layer. We retrieve a thickness of 0.45 ± 0.15 nm that agrees very well with the non-contact AFM measurement, namely 0.43 ± 0.25 nm; see Figs. 4(c) and 4(d). The uncertainty of 0.25 nm, which is comparable to the AFM noise level of 0.2 nm, is determined from the analysis of 510 data points measured at a substrate position without graphene. The contrast of the AFM image [see Fig. 4(a)] is lower than the one of the phase image due to a 1.7× larger noise. In addition to being at least 20× faster, the PIC-based QPI offers better noise performance compared to a standard AFM tool for this measurement. The theoretical thickness of the monolayer graphene specified by the supplier (Graphenea) is 0.34 nm, which corresponds to the interlayer spacing in graphite [46]. The value reported here is 30% larger, which is commonly observed with AFM measurement due to organic residues coming from the processing, adsorption of water molecules, and roughness of the substrate surface [47].

D. Quantitative Phase Mapping of Bacterial Cells

An important biological application of QPI is the identification of pathogens such as fungi cells or bacteria based on their shape and refractive index [48]. The optical throughput of our miniature PIC-based QPI approach in terms of lateral spatial

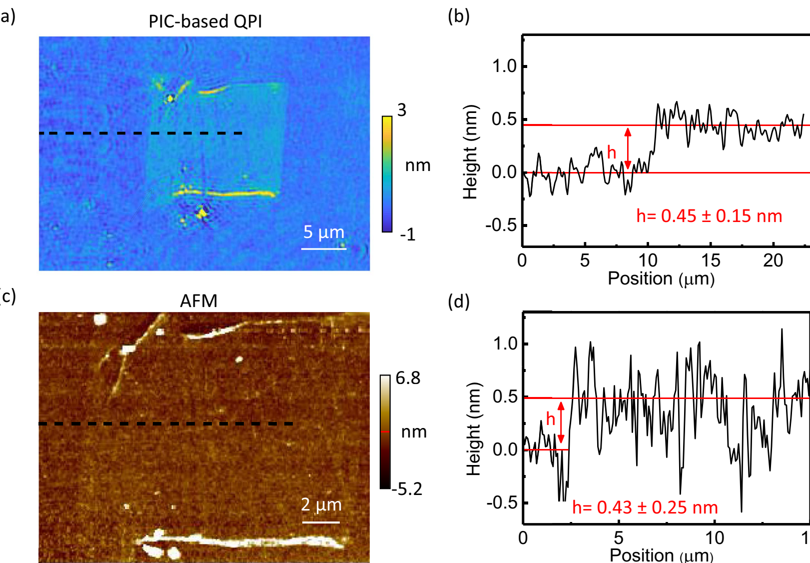

Fig. 4. Quantitative phase imaging of monolayer graphene. (a) Topographic image of a monolayer graphene patch measured with the PIC-based QPI (pixel size 100 nm). (b) Cross section along the dashed black line in (a). (c) Topographic image of the monolayer graphene patch measured by AFM (pixel size 78 nm). (d) Cross section along the dashed black line in (c). The cross section profiles are averaged over a vertical distance of 1.5 µm in both cases.

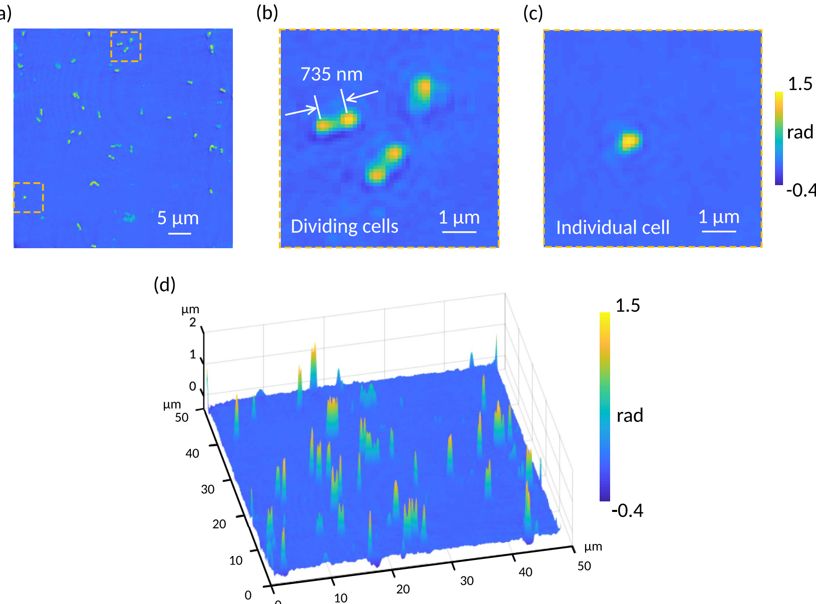

Fig. 5. Quantitative phase imaging of bacteria cells. (a) Phase image of *Escherichia coli* bacteria cells on a microscope cover glass. (b), (c) Zoom-in images of the area located in the dashed orange boxes showing the dividing cells and an individual cell, respectively. (d) 3D visualization of (a).

resolution and field of view is sufficiently high to discriminate different types of bacteria cells among large numbers as illustrated with *Escherichia coli* bacteria cells in Fig. 5. The lateral spatial resolution is large enough to distinguish individual cells from dividing cells for which a typical spacing between the nucleoids is 735 nm; see Fig. 5(b). Approximately 50 cells are visible within the field of view, a large majority of which exhibit a similar maximum phase; see Fig. 5(d). Lower phase entities are attributed to dead bacteria cells that have lost a fraction of their inner biological material. The miniature nature of the photonic chip and its phase imaging capability demonstrated on bacteria cells are promising for the deployment of compact imaging sensors to monitor the presence of pathogens in outdoor environments.

4. DISCUSSION

Our experimental results demonstrate that photonic integrated circuits are able to shape light beams to precisely match their far field with the numerical aperture of a microscope objective. The accuracy and robustness are such that quantitative phase imaging based on KK relations can be implemented with unprecedented performance for coherent light illumination. The PIC-based approach combines not only low phase noise of 5.5 mrad and high spatial resolution of 400 nm but also high compactness. As highlighted in Table 1, it outperforms recently reported state-of-the-art miniature modules for QPI based on metasurfaces [30,31], patterned microscope slides [29], or lensless optical fibers [49] by ∼2 times for spatial resolution and 15 times for phase noise. Besides, the detection limit of our PIC-based QPI is ∼7 times better than that obtained with the bulky optics approach based on the KK relations [40], is more than five times lower than that obtained with QPI techniques using a coherent light source (∼30 mrad), and is comparable to the best phase noise level obtained with the incoherent light sources (∼3 mrad) [32,34].

The performance of the PIC-based QPI represents a significant improvement compared to bulk optic approaches in view of the values of the temporal and spatial coherent length. The current laser linewidth of 50 pm and the spatial frequency broadening $\delta k = 0.122\ \mu m^{-1}$ correspond to a temporal coherence length of 2.6 mm and to a spatial coherence length of $l_s = 10\ \mu m$, respectively. With such values, Shin *et al.* have reported a phase noise around 100 mrad with a bulky optic setup [50], which is 18 times larger than the value achieved here with a photonic chip.

Table 1. Comparison of Miniature Modules for Quantitative Phase Imaging

Platform	Approach	Lateral Resolution	Spatial Phase Noise	Reference
Metasurface	Polarized light interference	2.76 µm	83 mrad[a]	[30]
Metasurface	Polarized light interference	2.13 µm	Unknown	[31]
Microscope slide	Digital holography	1.26 µm[b]	Unknown	[29]
Lensless fiber	Far-field speckle	1.0 µm	314 mrad[c]	[49]
PICs	KK relations	0.4 µm	5.5 mrad	This work

[a]This value is calculated according to the spatial noise of 36.9 ± 0.7 mrad/µm provided in Ref. [30].
[b]This resolution is calculated according to the working wavelength and objective used in Ref. [29].
[c]This value is the minimum phase measured in Ref. [49].

Shifting the working wavelength deeper into the UV can further improve the optical resolution, but with the appearance of more phototoxicity effects in biological samples. Phototoxicity effects, which cause irreversible damage to the DNA of biological cells [51], can be circumvented by decreasing the illumination dose and implementing a Hilbert–Huang transform. As recently demonstrated [52], the Hilbert–Huang transform is more robust to noise than the standard Hilbert transform, which allows reducing the UV photon budget without degrading the quality of the phase image.

The photonic chip used as a simple add-on miniature module provides the illumination of a standard wide-field optical microscope and upgrades the imaging system to a quantitative phase microscope. As a key result, topological profiles of quantitative phase images of graphene patches are obtained with a signal-to-noise ratio larger than 3 [see Fig. 4(b)], which enables us to clearly identify a single atomic monolayer. The phase image is retrieved from four single shot images with a 10 ms acquisition time. In this experiment, the thermal switch is stabilized for 30 s between each acquisition. The stabilization time is currently limited by the relative low efficiency of the thermal phase shifters, which can be further improved. The thermal phase shifter is one of the standard components in photonic integrated circuits and is well-developed in the silicon (Si) and silicon nitride (SiN) platforms where the switching rate can reach sub-kilohertz [53]. The AlO_x platform is at its early stage, and the thermo-optical coefficient of AlO_x is similar to that of SiN; consequently we expect significant improvement of the switching time of the phase shifters by engineering the heat dissipation or by developing UV compatible electro-optic approaches [39]. In addition to the temporal throughput, the spatial throughput of PIC-based QPI can be further enhanced by increasing the size of the diffraction gratings.

Dense integration of diverse optical functionalities is a key asset of photonic integrated circuits. The laser source integration on a single chip will make the system even more compact and stable, which has been demonstrated at telecom wavelengths [54]. In addition, a large number of diverse modalities can be integrated on a single photonics chip. For instance, simultaneously implementing on the same chip structured illumination microscopy (SIM), which we have demonstrated in Ref. [10], and quantitative phase imaging, as described here, will offer new imaging opportunities. Such multimodality imaging has the potential to improve the identification of pathogens in a lot of industrial processes or healthcare environments.

To conclude, the low phase noise demonstrated here with a compact photonic chip compatible with CMOS technology should accelerate the deployment of on-site quantitative phase imaging for a large number of biosensing and biomedical applications. In particular, the PIC-based QPI is expected to play a crucial role in hematological diagnosis and cancer pathology [55] by accelerating the diagnostic period and improving the diagnostic accuracy.

APPENDIX A

1. Necessary Conditions for Applying KK Relations

To apply the KK relations between $\ln(I(\vec{r}))$ and $\varphi(\vec{r})$, the function $\ln(E)$ has to be analytical, which requires some conditions. When the scattered field is weaker than the unscattered one, $|\frac{E_s}{E_u}| < 1$, for all positions in the image plane, the function $\ln(E)$ can be uniformly approximated by its Taylor development with respect to $E_s^N = \frac{E_s}{E_u}$. As a result, if E_s^N is an analytical signal, i.e., if a Hilbert transform exists between its real and imaginary parts, then $\ln(E)$ is also an analytical signal. The definition of a two-dimensional Hilbert transform poses uniqueness difficulties. Here, we consider only a one-dimensional Hilbert transform in the direction of illumination as in Ref. [16]. In order to define such a Hilbert transform, the field $E_s^N(x, y)$ must be extended holomorphically in the complex plane by replacing the real variable related to the direction of illumination by a complex number, $x + iv$, for instance. Expressing the field E_s^N as a function of its Fourier transform $\hat{E}_s^N$ as $E_s^N(x, y) = \int_{-\infty}^{+\infty} \hat{E}_s^N(k_x, y) e^{ik_x x} \mathrm{d}k_x$, the extended function $E_s^N(x + iv, y)$ is holomorphic if, in addition to being square integrable, $\hat{E}_s^N(k_x, y) = 0$ for $k_x < 0$. This condition that is similar to the causality condition in the time domain is imposed by the presence of the factor e^{-vk_x} that diverges for $k_x < 0$ and by an unambiguous definition of the Hilbert transform for $k_x = 0$ in the two-dimensional case; see condition (b) in Section 3 of Ref. [56]. It is in particular satisfied if $\hat{E}_s^N(k_x, k_y) = 0$ for $k_x < 0$. As illustrated in Fig. 1(b), an oblique illumination for which $k_{\mathrm{in}} = k_{\mathrm{max}}$ is in line with this last condition.

2. Description of the Image Post-Processing Algorithm

The MATLAB (R2023a) software is used to implement the algorithm that post-processes the intensity images in order to retrieve the phase images. The input files for the algorithm consist of intensity images obtained via PIC-based QPI measurements or three-dimensional finite-difference time-domain (FDTD) simulations. Four intensity images $I(\vec{r})$ are consecutively acquired with different illumination orientations that are symmetric under a rotation of 90 deg around the optical axis. As shown in Fig. 6, the image processing includes several steps. (1) Importing each intensity image, from which the intensity pattern of the illumination has been subtracted. (2) Defining an intermediate function $\chi(\vec{r}) = \ln(E(\vec{r}))$. The real part of the intermediate function $\chi(\vec{r})$ is obtained from the measured or simulated intensity images, $\mathrm{Re}(\chi(\vec{r})) = \frac{1}{2}\ln(I(\vec{r}))$. If the condition $\mathrm{NA}_{\mathrm{ex}} = \mathrm{NA}_{\mathrm{co}}$ is satisfied, the next step (3) applies Kramers–Kronig relations, or equivalently the Hilbert transform, to the function $\mathrm{Re}(\chi(\vec{r}))$ in order to retrieve the imaginary part $\mathrm{Im}(\chi(\vec{r}))$ [16]. Then, the complex light field $E(\vec{r})$ corresponding to the sum of the scattered and unscattered fields for a given $\vec{k}_{\mathrm{in}}$ illumination orientation is obtained by equation $E(\vec{r}) = e^{\frac{1}{2}\ln(I(\vec{r})) + iH(\frac{1}{2}\ln(I(\vec{r}))) + i\vec{k}_{\mathrm{in}}\vec{r}}$, where the $\vec{k}_{\mathrm{in}}$ is here the three-dimensional wave vector of the oblique illumination beam and the H denotes the Hilbert transform. In step (5), the light field is shifted by $-i\vec{k}_{\mathrm{in}}\vec{r}$ to its true position in the Fourier domain, namely the k-space. This can be achieved by multiplying the field $E(\vec{r})$ by $e^{-i\vec{k}_{\mathrm{in}}\vec{r}}$ in the space domain. After repeating the steps (1) to (5), the four complex field images corresponding to the four different orientations are determined. In step (6) these field images are then stitched in the

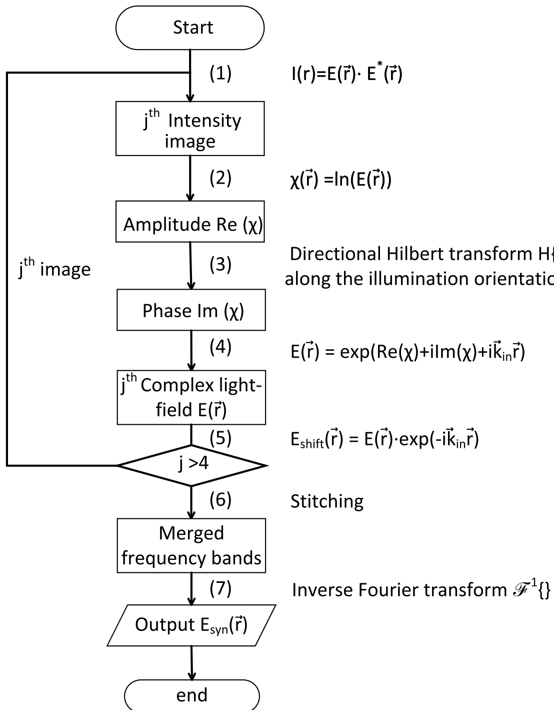

Fig. 6. Process flow of the algorithm to retrieve phase images by applying the Kramers–Kronig relations to intensity images.

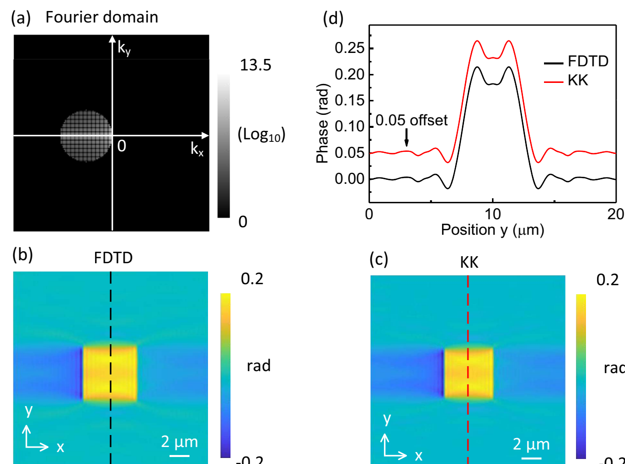

Fig. 7. Robust phase retrieval based on KK relations. (a) Log-scale Fourier domain of the field image of a square pillar object with an illumination orientation along d_1. (b) Phase image of a 50-nm-thick square pillar on cover glass, simulated using FDTD method. (c) Retrieved phase image of the object in (b) based on KK relations. (d) Cross section along the dashed lines in (b) and (c), respectively.

Fourier domain, which results in a synthetic complex field $\hat{E}_{\mathrm{syn}}(\vec{k})$ with the unscattered contribution located at a transverse wave vector $\vec{k} = \vec{0}$. (7) After applying an inverse fast Fourier transform, we obtain the amplitude image and the phase image of $\hat{E}_{\mathrm{syn}}(\vec{r})$. Note that the final retrieved phase image is associated with a given angle of illumination.

3. Simulating the KK-Based QPI Technique with FDTD Method

Simulation based on a three-dimensional FDTD method is performed to validate the QPI approach based on the KK relations. As shown in Fig. 7, a simple 50 nm thick square pillar with a size of 5 μm × 5 μm etched on a cover glass is used as a test object. The oblique illumination is oriented along d_1 as illustrated in the main text with an angle of $\theta = 26.74$ deg in the air. The angle corresponds to the maximum angle which can be collected by a microscope objective of NA = 0.45. A field monitor is placed at the top of the square pillar to collect the total field $E_{\mathrm{fdtd}}(\vec{r})$ transmitted by the object. A low-pass filter is applied to the image of this complex field to filter all the spatial frequencies outside the bandwidth of the microscope objective as illustrated in k-space for the amplitude of $\hat{E}_{\mathrm{fdtd}}(\vec{k})$ in Fig. 7(a). The band-limited phase image of the object [see Fig. 7(b)] is then extracted by taking the argument of the inverse Fourier transform of the complex field $\hat{E}_{\mathrm{fdtd}}(\vec{k})$. To retrieve the phase, the intensity image is used as input data for the post-processing algorithm. The result matches very well with the ground truth obtained directly by the FDTD method; see Figs. 7(b) and 7(c). To quantitatively compare Figs. 7(b) and 7(c), the cross sections of the phase image along the dashed lines are plotted in Fig. 7(d). The red curve is shifted by 0.05 rad along the vertical axis as otherwise it cannot be distinguished at all from the black curve. To conclude, the phase image retrieved with the KK-based QPI approach is identical to the phase image simulated with FDTD method, which validates the technique.

The divergence δ_{NA} [in units of NA: $\delta_{\mathrm{NA}} = \sin(\theta_{\max}) \frac{\delta k}{k_{\max}}$] of the beam impacts the value of the retrieved phase and consequently of the retrieved variations of the height of the object. An ideal plane wave is considered to apply the KK approach. However, the experimental illumination beam always has a certain degree of divergence due to the limited size of the diffraction gratings and waveguide loss. Here we simulate the impact of the beam divergence on the final phase images and topographical images. The topographical images that are obtained with two diverging beams of $\delta_{\mathrm{NA}} = 0.007$ and 0.015 are compared to the one obtained with an ideal plane wave; see Fig. 3(a). The cross sections along the dashed lines are plotted in Fig. 8(b) for quantitative comparison. The small oscillations in height come from sharp edge effects. The ratio between the retrieved height and the ground truth quantifies the impact of the beam divergence on the phase retrieval process; see Fig. 3(c). This impact is negligible for a divergence of $\delta_{\mathrm{NA}} = 0.007$, which corresponds to the experimental divergence provided by the photonic chip used in this work.

Since the method based on KK relations works only for a scalar system, the depolarization of the scattered light may also lead to inaccuracies in the phase retrieval process. To investigate this effect, we compare the application of the KK relations in two different cases, using simulated intensity images acquired with and without a linear polarizer. Linear polarizers are used to filter scattered light perpendicular to the polarization direction of the illumination beam. In the simulation, this can be achieved by keeping the relevant component of the electric field at the imaging plane and removing the rest. The intensity

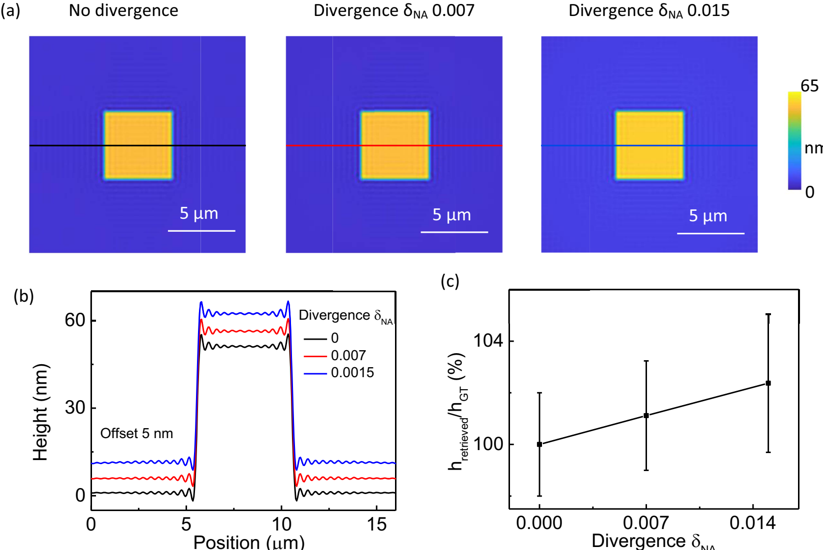

Fig. 8. Impact of the NA divergence on the retrieved topography. (a) Retrieved height images of a square pillar in the cases without beam divergence and with beam divergences δ_{NA} of 0.007 and 0.015, respectively. (b) Cross section along the solid lines in height images in (a). An offset of 5 nm along the y axis is set between the curves for better visualization. (c) Relationship between the height ratio of $h_{\mathrm{retrieved}}/h_{\mathrm{GT}}$ and beam divergence, where $h_{\mathrm{retrieved}}$ is the retrieved height and h_{GT} is the ground truth simulated with FDTD method. The error bars correspond to the distribution of the ripple fluctuations observed in (b).

images of the y- and x-axis polarized beams at the imaging plane are shown in Figs. 9(a) and 9(b), respectively. The intensity of the x-polarized scattered field is about 5 orders of magnitude lower than that of the y-polarized field, suggesting that the depolarization effect is negligible. To further confirm the negligible impact of the depolarization effects, we simulated the retrieved phase images with and without a polarizer as in the Fig. 1. Without a polarizer, the intensity image results from x-polarized and y-polarized fields $|(E_x)|^2 + |(E_y)|^2$, whereas with a polarizer, only fields having the same polarization as the illuminating beam contribute to the intensity image. In both cases, the topographical images retrieved from the phase images closely match the true topography of the object with a height of 50 nm. To quantify the differences, the solid line cross sections in Figs. 9(c) and 9(d) are plotted in Fig. 9(e). The difference in height between these two cases is in the order of 10^{-5} nm, which is negligible compared to the experimental resolution of the current technique.

4. Methodology for Beam Switching with a Photonic Integrated Circuit

To implement the QPI approach based on the KK relations, it is necessary to generate sequentially oblique beams that have different directions of illumination. This is achieved with a

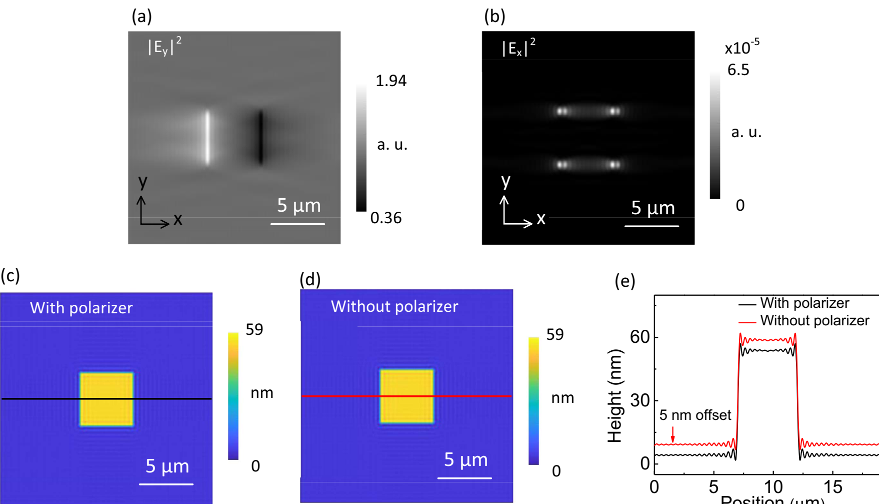

Fig. 9. Impact of depolarization on the retrieved topography. (a) Simulated intensity image of a square pillar obtained by using a linear polarizer along the y axis. The illumination beam is oriented along d_1, while its polarization is oriented along the y axis. (b) Simulated intensity image obtained with a linear polarizer along the x axis. (c), (d) Retrieved height images using intensity images acquired with and without a linear polarizer, respectively. (e) Height profiles along the solid lines in (c) and (d), respectively. A 5 nm offset is set for better visualization.

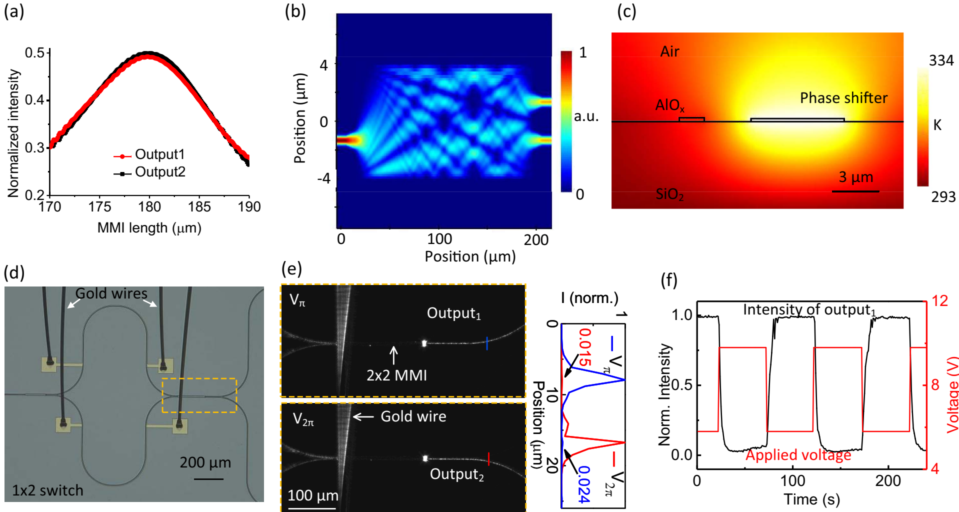

Fig. 10. On-chip beam switching. (a) Relationship between the intensity at outputs and the length of 2 × 2 multi-mode interferometer when a light source excites the fundamental transverse electric mode in one of the inputs. (b) Simulated light field propagating in the optimized MMI with one of the inputs being excited. (c) Heat transfer map of the on-chip thermal phase shifter. (d) Optical microscopy image of the 1 × 2 switch. (e) Optical image of the light propagation in a 1 × 2 switch when the applied voltages is V_π and $V_{2\pi}$, respectively. The plot shows the intensity profiles along the red and blue solid lines in the image. (f) Relationship between the scattered intensity of the output$_1$ in (d) and the voltage applied on the phase shifter(c) Heat transfer map of the on-chip thermal phase shifter. (d) Relationship between the scattered intensity of the output1 and the voltage applied on the phase shifter. The black curve shows the scattered intensity of the output1 in Fig. 2(c) in the main text, and the red curve shows the applied voltage.

1 × 4 on-chip switch and by positioning diffraction gratings in different directions. The key optical components of the 1 × 4 switch are 1 × 2 and 2 × 2 multimode interferometers (MMIs). In this work, the design and optimization of the MMIs are performed with the Eigen Mode Expansion (EME) method (Ansys Lumerical). The design of the 1 × 2 MMI has been optimized in our previous work [10]. Here, we focus on the design of the 2 × 2 MMI; see Figs. 10(a) and 10(b). The target is to design a 2 × 2 MMI that allows the powers of each input to be distributed equally between the two outputs in order to maximize the extinction ratio at each output. The input waveguide of the 2 × 2 MMI is tapered from 700 nm to 1.5 μm to minimize the insertion loss. The spacing between the input or output waveguides is one-third of the MMI width $W = 8$ μm. An optimum MMI length of 180 μm is selected to maximize the power at each output. The intensity profile of the beam propagating in the 2 × 2 MMI confirms the equal distribution of the power at the outputs in the case of the optimum MMI length; see Fig. 10(b).

Another important component of the switch is the thermal phase shifter. A spacing of 1.5 μm between the Au/Ti metal stack and the waveguide is selected to increase the modulation efficiency of the heater and meanwhile minimize the metal absorption. An electrical power of $P_\pi = 105$ mW heats up a 1-mm-long waveguide by 10.7°C and leads to a π-phase shift for the guided mode, which is simulated using finite element method (FEM) via COMSOL software. The π-phase shift of the guided mode allows us to switch on–off each output; see Figs. 10(d)–10(f). A high extinction ratio of 18.2 dB is experimentally achieved. The temporal throughput of the imaging technique currently depends on the switching rate of the phase shifter. Limited by the low thermal-optic coefficient of the AlO$_x$, the required P_π is relatively high, leading to a long rise time and fall time of 7 s; see Fig. 10(f). Unlike the bulky QPI technique based on the KK relationships where the electrical power consumption mainly comes from the galvanometer, with a typical value of about 20 W, the PIC-based approach consumes only 0.315 W, a 63-fold improvement in power efficiency achieved through the use of on-chip beam switching.

The field of view (FoV) of the illumination is a critical factor in determining the special throughput of the imaging technique. With the current chip design, the FoV amounts to 210 μm × 187 μm for each illumination beam; see Fig. 11.

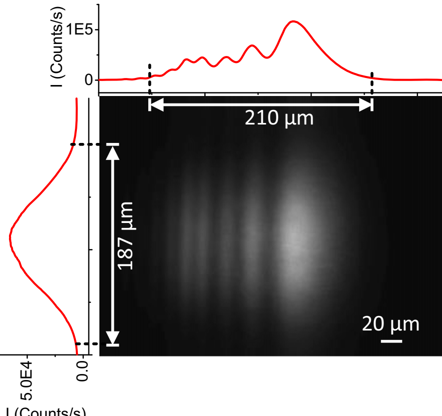

Fig. 11. Intensity profile of the illumination beam. Intensity image of a typical diffracted beam at the object plane. The intensity profiles along the x and y axes are summed on the top and left side of the image, respectively.

The field of view of the illumination beam can be further improved by increasing the length and width of the diffraction grating, but at the cost of a longer adiabatic taper to guarantee single-mode guidance. With the current CCD camera (Thorlabs 340USB: 640 pixels × 5480 pixels, pixel size is 7.4 μm) and the microscope objective of NA = 0.45, the maximum FoV for the light collection is 128 μm × 96 μm to keep the best spatial resolution of 400 nm. It corresponds to a transverse magnification of 37. The experimental images reported here have been oversampled by a factor of approximately two (magnification 74) [see Fig. 12 and in particular the *k*-space in Fig. 12(b)], which limits the FoV for the collection to 64 μm × 48 μm.

5. Methodology to Process the Experimental Images in *k*-Space

In this note we present the different steps required to produce the quantitative phase images by using the KK relations. A pure phase object made of standard microscope cover glass is used as a test object. The strip patterns are etched with a nominal height of 46.7 nm, and the different spacings between the strips allow us to determine the optical resolution of the PIC-based QPI technique. The intensity images are acquired sequentially by switching the beam from d_1 to d_4; see Fig. 12(a). Their corresponding Fourier transform images are presented in log-scale in Fig. 12(b). When the spatial frequency of the oblique illumination beam $\frac{2\pi}{\lambda}\mathrm{NA}_{\mathrm{ex}}$ matches the maximum frequency collected by the microscope objective $\frac{2\pi}{\lambda}\mathrm{NA}_{\mathrm{co}}$, the frequency bands indicated by two solid red circles intersect only at the origin and are otherwise separated. This fulfills the condition to retrieve the phase images with the KK relations. After performing an inverse Fourier transform on the merged frequency bands [see Fig. 12(c)], we obtain both the amplitude and phase images of the object; see Figs. 12(d) and 12(e), respectively. The topographical images, zooming in on the 300, 400, and 600 nm strips, are shown in Figs. 3(a) and 3(b) in the main text.

6. Methodology to Determine the Object Topography from Phase Images

The phase image shows the phase delay introduced by the object at a given plane. With a standard illumination parallel to the optical axis of the microscopy objective, the phase delay is related to the optical path difference (OPD) between the situation with and without the object and, neglecting edge effects, is given by $\Delta\varphi = \frac{\Delta n h}{\lambda}$, where Δn is the difference between the refractive indices of the object and environment, h is the thickness of the object, and λ is the working wavelength. In the case of an oblique illumination, the illumination angle θ plays a role in the phase delay as shown in Fig. 13. In this figure, a tilted beam with an angle θ_1 is incident at the bottom of the object. Without the presence of the object, the beam propagates along a straight path from point O to point C. The optical path difference between the point O and C is written as $\mathrm{OPD}_{\mathrm{OC}} = \frac{h}{\cos(\theta_1) n_1}$, where $n_1 = 1$ in the air. With the presence of the object, the refraction of the light occurs and leads to a change of the propagation path. The beam that passes through position A is refracted at B and reaches point C. As a result, the optical path difference between points A and C is given by $\mathrm{OPD}_{\mathrm{ABC}} = hn_1(\tan(\theta_1) - \tan(\theta_2))\sin(\theta_1) + \frac{h}{\cos(\theta_2)} n_2$. Considering Snell's

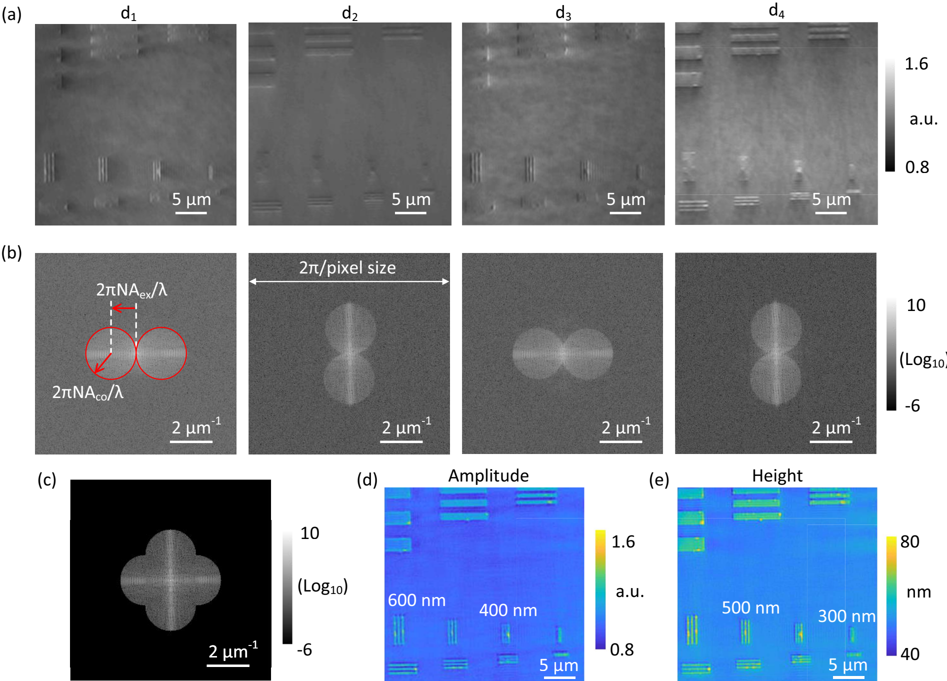

Fig. 12. Image processing steps. (a) Measured optical intensity images illuminated with oblique beams along the orientation d_1–d_4. (b) Log-scale fast Fourier transform of the intensity images in (a). (c) Log-scale amplitude image of merged light field in Fourier domain. (d) Retrieved amplitude image. (e) Retrieved height image.

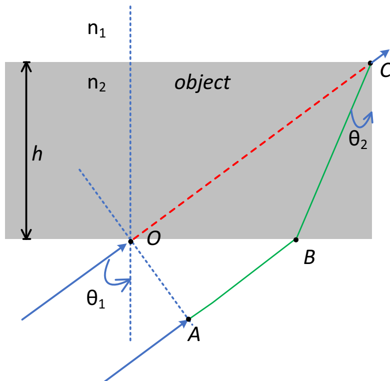

Fig. 13. Schematic of the phase delay for oblique illumination. h, height of the object; n_1, n_2, refractive indices of the environment and object, respectively. The beam that is incident with an angle of θ_1 is refracted with an angle θ_2 inside the object. Red dashed line: optical path without object.

law, $n_1 \sin(\theta_1) = n_2 \sin(\theta_2)$, we can obtain the phase delay introduced by the object: $\Delta\varphi = \mathrm{OPD}_{\mathrm{ABC}} - \mathrm{OPD}_{\mathrm{OC}} = \frac{2\pi}{\lambda} h(n_2 \cos(\theta_2) - n_1 \cos(\theta_1))$. This equation shows that the phase delay of the oblique beam depends not only on the n value and height h of the object but also on the angle θ of the illumination. By knowing the n values, the angle, and the working wavelength of the illumination beam, the height of the object h is determined from the retrieved phase for positions several wavelengths away from abrupt variations of the topography, i.e., where edge effects take place.

7. Methodology to Achieve High-Precision Control of Beam Angles Using Photonic Integrated Circuits

The precise NA matching between the illumination beam and microscope objective plays a vital role in the implementation of the KK relations. In practice, the NA mismatch unavoidably occurs because of the imperfection during the fabrication of PICs, the parameter deviation in simulation, or the misalignment of optical components. To investigate the effects of NA mismatch in the implementation of the KK relations, we have studied different oblique beams with varying $\mathrm{NA}_{\mathrm{ex}}$ values close to the $\mathrm{NA}_{\mathrm{co}}$ value and have compared the retrieved phase to its real phase; see Fig. 14. The $\mathrm{NA}_{\mathrm{ex}}$ values with a step of 0.005 are controlled by the on-chip diffraction gratings. A difference of 1 nm in grating pitch as shown in Fig. 14(a) corresponds to an $\mathrm{NA}_{\mathrm{ex}}$ variation of 0.01. Besides, changing the filling factor from 0.8 to 0.6 leads to an $\mathrm{NA}_{\mathrm{ex}}$ variation of 0.005. By sweeping both the filling factor and grating pitch, we achieved a high-precision sweep of $\mathrm{NA}_{\mathrm{ex}}$ with a step of 0.005 corresponding to NA mismatch steps of 1.1%. The square pillars used as a test object have a height of 24.9 nm according to the histogram plot of the AFM image in Fig. 14(b). The surface roughness RMS of the substrate after etching is estimated to be 5 nm. After acquiring intensity images and implementing PIC-based QPI technique, the topographical images are obtained from the retrieved phase image using the approach described above; see Fig. 14(c). The object height is estimated from the spacing

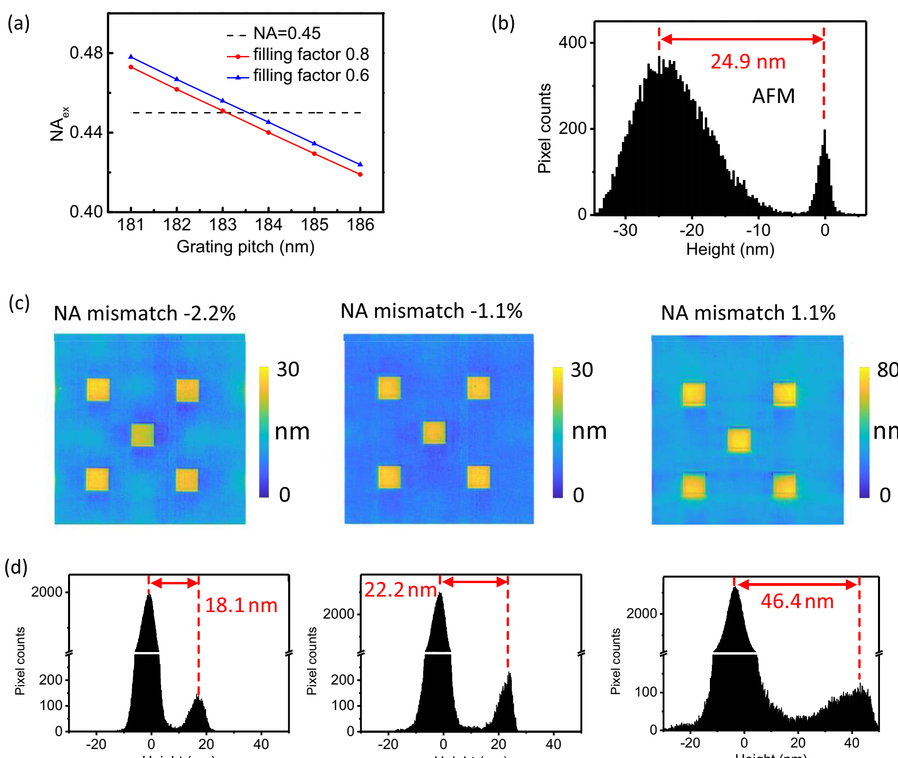

Fig. 14. Impact of the NA mismatch. (a) Relationship between the grating pitch and the numerical aperture $\mathrm{NA}_{\mathrm{ex}}$ of the diffracted beam for filling factors of 0.6 and 0.8, respectively. (b) Histogram plot of the height profile of a square pillar measured by AFM in Fig. 2(e) in the main text. (c) Height images of the same object in (b), retrieved with PIC-based QPI for different NA mismatches. The NA mismatch is defined as $(\mathrm{NA}_{\mathrm{ex}}\text{-}\mathrm{NA}_{\mathrm{co}})/\mathrm{NA}_{\mathrm{co}}$ and given in percentage. (d) Histogram plots corresponding to the images in (c).

between the peaks in the corresponding histogram plots of the topographical images; see Fig. 14(d). The data in Fig. 14 complement those in Fig. 2. As expected, the NA mismatch leads to an inaccuracy of the phase retrieval in the implementation of the KK relations.

8. Device Fabrication and Measurement

The fabrication of AlO_x-PICs is compatible with CMOS technology and is divided into three main steps including full-etch of the waveguides, shallow-etch of the gratings, and metallization of the thermal phase shifters. Fabrication details refer to our previous work in Ref. [10].

The pure phase objects are made of either microscope cover glasses or SiO_x layers deposited on microscope cover glasses. These samples have high transparency at a working wavelength of 360 nm. The cover glass samples are ultrasonically cleaned for 10 min in an acetone solution before use. The SiO_x on cover glass sample consists of a 500 nm thick layer of SiO_x deposited with plasma enhanced chemical vapor deposition (PECVD). To pattern the surface of the samples, a layer of 200 nm thick photoresist (ARP6200.09, Allresist) is spin-coated on the sample (4000 r/min, 60 s) and baked (150°C, 1 min). A layer of Electra 92 is then applied and baked at 90°C for 2 min to improve the conductivity. The patterns are defined on a photoresist layer using an e-beam lithography (EBL) system that is then developed in n-amyl acetate for 60 s. The pattern defined in the photoresist layer is transferred to the glass substrate or SiO_x layer by dry-etching with a fluorine-based gas mixture of CF_4/Ar in a reactive ion etcher (RIE).

The bacterial strains are ordered from DSMZ (Braunschweig, Germany) and cultured for 24 h in nutrient broth at 28°C. A droplet of the bacterial solution is dropped directly onto a glass substrate before being imaged by the PIC-based QPI.

The graphene sample presented in Fig. 4 was prepared using a conventional transfer printing technique. To precisely locate the graphene patches during both the AFM and optical measurements, we first fabricated markers on a cover glass substrate. Initially, a 200 nm thick layer of photoresist was coated on the glass substrate. Electron beam lithography was then employed to expose the photoresist, and, after development, the marker structures were etched onto the glass substrate using fluorine-based gases in RIE. Meanwhile, we patterned a single-layer graphene flake on a SiO_2/Si substrate (Graphenea) using EBL. This was followed by a 3-min oxygen plasma process to etch the graphene layer. Then, these single-layer graphene flakes were transferred to the glass substrate in the region pre-patterned with markers. This was accomplished using a poly-(methyl methacrylate) (PMMA)-assisted transfer process. In detail, the SiO_2/Si substrate with graphene flakes was spin-coated with a PMMA support layer (1500 r/min, 3 min) and baked on a hot plate at 150°C for 1 min. To improve adhesion, a solid film of polydimethylsiloxane (PDMS) was carefully attached to the PMMA layer and heated on a hot plate at 80°C for 1 min. The PDMS/PMMA/graphene stack was then separated from the substrate using a water droplet due to the hydrophobic nature of PMMA. Finally, the PDMS/PMMA/graphene stack was positioned on a glass slide to ensure precise alignment with the marker region on the target glass substrate.

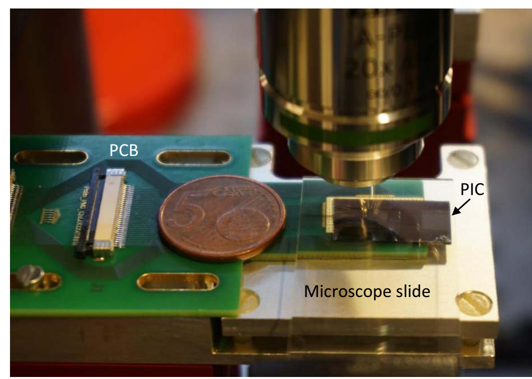

Fig. 15. Photograph of the PIC-based QPI setup. PIC, photonic integrated circuit; PCB, printed circuit board. The diameter of the 5-cent Euro is 21.25 mm.

This transfer step is performed with micrometer precision in a home-made stamping setup, where the PDMS sheet is detached from the PMMA/graphene layer at 150°C. Finally, the PMMA film is removed by soaking the target substrate in acetone overnight.

The acquisition of the intensity images of the objects is performed at a working wavelength of 360 nm. A continuous-wave UV solid-state laser source (CNIlaser, UV-F-360) provides a maximum power of 50 mW in free space and a spectral linewidth of 50 pm. The laser beam is expanded and coupled from free space to a single-mode fiber (SM300). The maximum optical power collected at the fiber output is 24 mW. During the measurement, only 4 mW of optical power was used to excite the photonic circuit in order to avoid camera saturation. Each grating provides an irradiance of 50 μW, which enables a fast acquisition of the intensity images with a 10 ms integration time. The photonic chip was maintained at room temperature during the measurement using a Peltier temperature controller. Alignment of the photonic chip relative to the optical imaging microscope is important to obtain an NA match between the illumination and collection and therefore good phase image fidelity. During the alignment process, the 1×4 switch is set to activate all diffraction gratings in order to simultaneously diffract the four beams in the far field. The NA mismatch caused by the misalignment of the photonic chip will result in a partial cut of the beam profiles when they are imaged in the real space domain, namely at the imaging plane. With the photonic chip aligned, the intensity profiles of the diffracted beams that are imaged in the conventional real space are circularly symmetric along the optical axis of the microscope objective without being (partially) blocked. To calibrate the actual spatial frequency of the intensity image in the Fourier space domain (k-space), the maximum spatial frequency $k_{\max}$ that can be collected by the microscope objective is used as a reference. The clear boundary of the objective aperture is illuminated by a light emitting diode, as shown in Figs. 2(b) and 2(c).

Figure 15 shows a photograph of the PIC-based QPI setup. A 5-cent Euro coin with a diameter of 21.25 mm is used as the scale reference for the system.

Funding. Fonds Wetenschappelijk Onderzoek (G033722N, S008421N); Bijzonder Onderzoeksfonds UGent (01IO1320).

Acknowledgment. C.L. and N.L.T. acknowledge Christophe Detavernier's research team for providing the ALD AlO_x layers, Nico Boon for providing biological samples, and Tom Vandekerckhove for helping to measure the samples with the AFM.

Disclosures. The authors declare no conflicts of interest.

Data Availability. Data underlying the results presented in this paper are not publicly available at this time but may be obtained from the authors upon reasonable request.

REFERENCES

1. J. W. Goodman, *Introduction to Fourier Optics* (McGraw-Hill, 2005).
2. F. M. Dickey and S. C. Holswade, *Laser Beam Shaping Theory and Techniques* (Marcel Dekker, 2000).
3. K. Van Acoleyen, W. Bogaerts, J. Jágerská, *et al.*, "Off-chip beam steering with a one-dimensional optical phased array on silicon-on-insulator," Opt. Lett. **34**, 1477–1479 (2009).
4. J. Sun, E. Timurdogan, A. Yaacobi, *et al.*, "Large-scale nanophotonic phased array," Nature **493**, 195–199 (2013).
5. C. V. Poulton, A. Yaacobi, D. B. Cole, *et al.*, "Coherent solid-state LIDAR with silicon photonic optical phased arrays," Opt. Lett. **42**, 4091–4094 (2017).
6. F. Ashtiani, A. J. Geers, and F. Aflatouni, "An on-chip photonic deep neural network for image classification," Nature **606**, 501–506 (2022).
7. C. M. Gentry, M. Bagnell, S. Cook, *et al.*, "Large, wafer-thin optical apertures leveraging photonic integrated circuits to replace telescopes for communications," in *37th Annual Small Satellite Conference* (2023), paper SSC23-IX-01.
8. O. I. Helle, F. T. Dullo, M. Lahrberg, *et al.*, "Structured illumination microscopy using a photonic chip," Nat. Photonics **14**, 431–438 (2020).
9. R. Diekmann, Ø. I. Helle, C. I. Øie, *et al.*, "Chip-based wide field-of-view nanoscopy," Nat. Photonics **11**, 322–328 (2017).
10. C. Lin, J. S. D. Peñaranda, J. Dendooven, *et al.*, "UV photonic integrated circuits for far-field structured illumination autofluorescence microscopy," Nat. Commun. **13**, 4360 (2022).
11. C. Lin, D. Schaubroeck, R. Baets, *et al.*, "UV photonic-integrated-circuits-based structured illumination microscopy with a field of view larger than 100 μm^2," IEEE J. Sel. Top. Quantum Electron. **29**, 7100709 (2023).
12. K. K. Mehta, C. Zhang, M. Malinowski, *et al.*, "Integrated optical multi-ion quantum logic," Nature **586**, 533–537 (2020).
13. S. Sharif Azadeh, J. C. C. Mak, H. Chen, *et al.*, "Microcantilever-integrated photonic circuits for broadband laser beam scanning," Nat. Commun. **14**, 2641 (2023).
14. A. Mohanty, Q. Li, M. A. Tadayon, *et al.*, "Reconfigurable nanophotonic silicon probes for sub-millisecond deep-brain optical stimulation," Nat. Biomed. Eng. **4**, 223–231 (2020).
15. D. L. Misell and A. H. Greenaway, "An application of the Hilbert transform in electron microscopy: I. Bright-field microscopy," J. Phys. D **7**, 832–855 (1974).
16. Y. Baek and Y. Park, "Intensity-based holographic imaging via space-domain Kramers-Kronig relations," Nat. Photonics **15**, 354–360 (2021).
17. Y. Park, C. Depeursinge, and G. Popescu, "Quantitative phase imaging in biomedicine," Nat. Photonics **12**, 578–589 (2018).
18. G. Popescu, T. Ikeda, R. R. Dasari, *et al.*, "Diffraction phase microscopy for quantifying cell structure and dynamics," Opt. Lett. **31**, 775–777 (2006).
19. P. Bon, G. Maucort, B. Wattellier, *et al.*, "Quadriwave lateral shearing interferometry for quantitative phase microscopy of living cells," Opt. Express **17**, 13080–13094 (2009).
20. T. Kim, R. Zhou, M. Mir, *et al.*, "White-light diffraction tomography of unlabelled live cells," Nat. Photonics **8**, 256–263 (2014).
21. N. T. H. Nguyen, M. E. Kandel, M. Rubessa, *et al.*, "Gradient light interference microscopy for 3D imaging of unlabeled specimens," Nat. Commun. **8**, 210 (2017).
22. P. Marquet, B. Rappaz, P. J. Magistretti, *et al.*, "Digital holographic microscopy: a noninvasive contrast imaging technique allowing quantitative visualization of living cells with subwavelength axial accuracy," Opt. Lett. **30**, 468–470 (2005).
23. W. Choi, C. Fang-Yen, K. Badizadegan, *et al.*, "Tomographic phase microscopy," Nat. Methods **4**, 717–719 (2007).
24. G. Popescu, L. P. Deflores, J. C. Vaughan, *et al.*, "Fourier phase microscopy for investigation of biological structures and dynamics," Opt. Lett. **29**, 2503–2505 (2004).
25. G. Zheng, R. Horstmeyer, and C. Yang, "Wide-field, high-resolution Fourier ptychographic microscopy," Nat. Photonics **7**, 739–745 (2013).
26. F. E. Robles, "Epi-mode tomographic quantitative phase imaging in thick scattering samples," Proc. SPIE **11251**, 112511Y (2020).
27. H. Zhou, E. Stoykova, M. Hussain, *et al.*, "Performance analysis of phase retrieval using transport of intensity with digital holography," Appl. Opt. **60**, A73–A83 (2021).
28. L. Wesemann, J. Rickett, J. Song, *et al.*, "Nanophotonics enhanced coverslip for phase imaging in biology," Light Sci. Appl. **10**, 98 (2021).
29. V. Bianco, B. Mandracchia, V. Marchesano, *et al.*, "Endowing a plain fluidic chip with micro-optics: a holographic microscope slide," Light Sci. Appl. **6**, e17055 (2017).
30. H. Kwon, E. Arbabi, S. M. Kamali, *et al.*, "Single-shot quantitative phase gradient microscopy using a system of multifunctional metasurfaces," Nat. Photonics **14**, 109–114 (2019).
31. Q. Wu, J. Zhou, X. Chen, *et al.*, "Single-shot quantitative amplitude and phase imaging based on a pair of all-dielectric metasurfaces," Optica **10**, 619–625 (2023).
32. B. Bhaduri, C. Edwards, H. Pham, *et al.*, "Diffraction phase microscopy: principles and applications in materials and life sciences," Adv. Opt. Photonics **6**, 57–119 (2014).
33. B. Bhaduri, H. Pham, M. Mir, *et al.*, "Diffraction phase microscopy with white light," Opt. Lett. **37**, 1094–1096 (2012).
34. G. Baffou, "Wavefront microscopy using quadriwave lateral shearing interferometry: from bioimaging to nanophotonics," ACS Photonics **10**, 322–339 (2023).
35. Z. Wang, L. Millet, M. Mir, *et al.*, "Spatial light interference microscopy (SLIM)," Opt. Express **19**, 1016–1026 (2011).
36. E. C. Titchmarsh, *Introduction to the Theory of Fourier Integrals* (Chelsea, 1986).
37. M. M. Aslan, N. A. Webster, C. L. Byard, *et al.*, "Low-loss optical waveguides for the near ultra-violet and visible spectral regions with Al_2O_3 thin films from atomic layer deposition," Thin Solid Films **518**, 4935–4940 (2010).
38. C. Franken, W. Hendriks, M. Dijkstra, *et al.*, "First near-UV hybrid integrated laser in the Al_2O_3 platform," Proc. SPIE **PC12424**, PC124240A (2023).
39. G. N. West, W. Loh, D. Kharas, *et al.*, "Low-loss integrated photonics for the blue and ultraviolet regime," APL Photonics **4**, 026101–026107 (2019).
40. C. Lee, Y. Baek, H. Hugonnet, *et al.*, "Single-shot wide-field topography measurement using spectrally multiplexed reflection intensity holography via space-domain Kramers-Kronig relations," Opt. Lett. **47**, 1025–1028 (2022).
41. K. F. Mak and J. Shan, "Photonics and optoelectronics of 2D semiconductor transition metal dichalcogenides," Nat. Photonics **10**, 216–226 (2016).
42. Z. Lin, Y. Liu, U. Halim, *et al.*, "Solution-processable 2D semiconductors for high-performance large-area electronics," Nature **562**, 254–258 (2018).
43. S. M. Koepfli, M. Baumann, Y. Koyaz, *et al.*, "Metamaterial graphene photodetector with bandwidth exceeding 500 gigahertz," Science **380**, 1169–1174 (2023).
44. Y. Guo, Z. Xu, A. G. Curto, *et al.*, "Plasmonic semiconductors: materials, tunability and applications," Prog. Mater. Sci. **138**, 101158 (2023).

45. M. A. El-Sayed, G. A. Ermolaev, K. V. Voronin, *et al.*, "Optical constants of chemical vapor deposited graphene for photonic applications," Nanomaterials **11**, 1230 (2021).
46. R. Heyrovska, "The coulombic nature of the van der Waals bond connecting conducting graphene layers in graphite," Graphene **05**, 35–38 (2016).
47. Z. Shen, J. Li, M. Yi, *et al.*, "Preparation of graphene by jet cavitation," Nanotechnology **22**, 365306 (2011).
48. G. Kim, D. Ahn, M. Kang, *et al.*, "Rapid species identification of pathogenic bacteria from a minute quantity exploiting three-dimensional quantitative phase imaging and artificial neural network," Light Sci. Appl. **11**, 190 (2022).
49. J. Sun, J. Wu, S. Wu, *et al.*, "Quantitative phase imaging through an ultra-thin lensless fiber endoscope," Light Sci. Appl. **11**, 204 (2022).
50. S. Shin, K. Kim, K. Lee, *et al.*, "Effects of spatiotemporal coherence on interferometric microscopy," Opt. Express **25**, 8085–8097 (2017).
51. B. J. Zeskind, C. D. Jordan, W. Timp, *et al.*, "Nucleic acid and protein mass mapping by live-cell deep-ultraviolet microscopy," Nat. Methods **4**, 567–569 (2007).
52. X. Chang, C. Shen, S. Liu, *et al.*, "Robust Kramers-Kronig holographic imaging with Hilbert-Huang transform," Opt. Lett. **48**, 4161–4164 (2023).
53. Z. Yong, H. Chen, X. Luo, *et al.*, "Power-efficient silicon nitride thermo-optic phase shifters for visible light," Opt. Express **30**, 7225–7237 (2022).
54. G. Roelkens, J. Zhang, L. Bogaert, *et al.*, "Present and future of micro-transfer printing for heterogeneous photonic integrated circuits," APL Photonics **9**, 010901 (2024).
55. H. Majeed, S. Sridharan, M. Mir, *et al.*, "Quantitative phase imaging for medical diagnosis," J. Biophotonics **10**, 177–205 (2017).
56. J. P. Havlicek, J. W. Havlicek, and A. C. Bovik, "The analytic image," in *Proceedings of International Conference on Image Processing* (1997), Vol. **2**, pp. 446–449.

157.193.240.1 {ts '2024-12-12 14:58:12'}